Article

Simulation Study of the Lunar Spectral Irradiances and the Earth-Based Moon Observation Geometry

Yi Lian * , Qianqian Renyang , Tianqi Tang * , Hu Zhang , Jinsong Ping , Zhiguo Meng , Wenxiao Li ,
Huichun Gao

Posted Date: 21 July 2023

doi: 10.20944/preprints202307.1508.v1

Keywords: Lunar spectral irradiances; Earth-based Moon observation geometry; Hapke model

Article

Simulation Study of the Lunar Spectral Irradiances and the Earth-Based Moon Observation Geometry

Yi Lian [1,2,*], Qianqian Renyang [1], Tianqi Tang [3,*], Hu Zhang [1], Jinsong Ping [2], Zhiguo Meng [2,3], Wenxiao Li [2] and Huichun Gao [1]

[1] Tianjin Normal University, College of Geography and Environmental Sciences, Tianjin 300387, China
[2] National Astronomical Observatory of the Chinese Academy of Sciences, Beijing 100012, China
[3] Jilin University, Changchun 130012, China
* Correspondence: lianyi@tjnu.edu.cn(Y.L.); tangtq20@mails.jlu.edu.cn(T.T.)

Abstract: The radiant energy of the Moon is in the dynamic range of most payloads, so the Moon is a good light source for the on-orbit radiometric calibration of the spacecraft. The key to the calibration is the simulation of the lunar spectral irradiances and the Earth-based Moon observation geometry. In this paper, the Hapke model would be used to simulate the lunar spectral irradiances at the observation time using the data of based on Lunar Reconnaissance Orbiter Camera (LROC) products. The projection transformation from the lunar geographic coordinate system to the instantaneous projection coordinate system was made to establish the observation geometry. It is expected that the conclusion drawn in this paper support for on-orbit calibration of spacecraft in the future.

Keywords: lunar spectral irradiances; earth-based moon observation geometry; Hapke model

1. Introduction

Satellite radiometric calibration is the basis and key to remote sensing quantification. Countries around the world attach great importance to satellite calibration and have developed a variety of calibration methods, such as laboratory calibration, field calibration, and cross-calibration [1,2]. Laboratory calibration cannot represent the operation of satellites in orbit. Field calibration is affected by atmospheric scattering and absorption, geometric differences between ground measurements and satellite observations, and scale differences between ground measurement points and satellite measurement points. In addition, for remote sensing, the influence of the atmosphere on the calibration is relartive large. Unlike the Earth, the Moon has essentially no atmosphere and its reflectance is very stable hence it is good radiance source for the calibration of space crafts. For visible spectral remote sensing, the reflectance of the moon is very stable, and the spectral curve is smooth. For thermal infrared remote sensing, the specific emissivity of the moon is very large, similar to a black body. Therefore, whether it is short-wave or long-wave remote sensing, the moon is a good light source for on-orbit radiation calibration and stability monitoring [3,4] .

There has been a great deal of research on lunar calibration [5–9]. At present, many satellites have carried out observation experiments on the moon with various payloads, such as MODIS [10], Hyperion [11], GOES [12], SeaWiFS [13,14], S-NPP [15], Hodoyoshi-1 [16] and FY meteorological satellite [17], etc. These observations have laid a good foundation for satellite calibration using the moon as a calibration source. In this paper, we simulatethe distribution of the lunar spectral irradiances at the observation time, which is influenced by the phase of the Moon, the libration, and the distance between the Sun, Earth and the Moon. There are two key main question in our research question including the lunar spectral irradiances simulation and a projection transformation from the lunar geographic coordinate system to an instantaneous projection coordinate system. The Hapke bidirectional reflectance function can be used to simulate the lunar spectral irradiances at the observation time by using Lunar Reconnaissance Orbiter Camera (LROC) products. The projection in an instantaneous projection coordinate system can establish a mapped relationship between transformation from the lunar geographic coordinate system and the instantaneous projection coordinate system at the observation time. It is expected that the conclusion drawn in this paper support for on-orbit calibration of spacecraft in the future.

2. Materials and Methods

2.1. Data and Coordination system

2.1.1. Data Collection

In June 2009, NASA launched the Lunar Reconnaissance Orbiter(LRO), a robotic spacecraft, now orbiting the Moon at an altitude of 50-200 km. The LROC, one of the instruments on board LRO, is provided to construct the lunar global multi-spectral map[18] including 321, 360, 415, 566, 604, 643, and 689 nm. Global multispectral observations in seven wavelengths could be used to characterize lunar resources, in particular ilmenite. Some products of LROC including LROC Empirically Normalized Wide Angle Camera Mosaic Data Record (MDREMP), LROC Special Data Record Hapke Photometric Parameter Maps (SDWHAP) would be used in our research.

The SDWHAP consisted of 9 Hapke parameters (w, b, c, Bc0, hc, Bs0, hs, theta, phi) for each of the 7 bands of the Wide Angle Camera (WAC) in Equirectangular projection (centered at 0°N, 0°E; 1° by 1° pixel scale)[19]. Spatially resolved near-global Hapke photometric parameter maps of the Moon from ~66,000 LROC WAC multispectral observations acquired from February 2010 to October 2011. Maps extend 0°E-360°E, 70°N-70°S. These maps could be used to normalize the simulated reflectance at standard angles in 1° latitude by 1° longitude tiles in this research.

The MDREMP empirically normalized WAC mosaic was constructed from 137,400 colour WAC images acquired from January 21, 2010, to January 31, 2013, over a broad range of lighting and viewing geometries[20]. Each pixel from the WAC observations was photometrically normalized to a standard geometry of 30-degree incidence angle, 0-degree emission angle, and 30-degree phase angle using an empirically derived global photometric function. Normalized WAC pixels for each location were combined using the median (average n=142), so each mosaic value is using information from many observations.

The SORCE SIM Solar Spectral Irradiance (SSI) data product SORCE SIM Level 3 Solar Spectral Irradiance Daily Means V027 (SOR3SIMD) would be used in the research as the estimation product of solar radiation energy[21]. The SOR3SIMD is constructed using measurements from the SIM instruments, which are combined into merged daily solar spectra over the spectral range from 240 to 2416 nm at a spectral resolution ranging from 1 to 27 nm. Irradiances are reported at a mean solar distance of 1 AU and zero relative line-of-sight velocity to the Sun. The SIM absolute uncertainty is about 2%. All of the SOR3SIMD data are arranged in a single file in a tabular ASCII text file which can be easily read into a spreadsheet application. The columns contain the date, Julian day, minimum wavelength, maximum wavelength, instrument mode, data version number, irradiance value, irradiance uncertainty, and data quality. The rows are arranged with data at each wavelength over the full SIM wavelength range, repeating each day for the length of the measurement period.

2.1.2. The basic coordinate system

1. The lunar geographic coordinate system;

The lunar geographic coordinate system is commonly used for lunar mapping, similar to the Earth's geographic coordinate system. The lunar geographic coordinate system uses a three-dimensional spherical surface to define locations on the moon. The lunar geographic coordinate system includes an angular unit of measure, a prime meridian, and a datum (based on a spheroid). The origin of the coordinates is the centre of the lunar reference ellipsoid and the reference plane is the spherical reference ellipsoid sphere. The basic plane includes the lunar prime meridian and the equatorial plane. Latitude values (B) are measured relative to the equator and range from –90° at the south pole to +90° at the north pole. Longitude values (L) are measured relative to the prime meridian and range from –180° when travelling west to 180° when travelling east. The elevation (H) is defined by the distance from the reference point of the reference ellipsoid normal to the reference ellipsoid.

doi:10.20944/preprints202307.1508.v1

The position of any point (A) on the moon is referenced by its longitude, latitude and elevation values in the lunar geographic coordinate system (Figure 1(**a**)) as (B, L, H) .

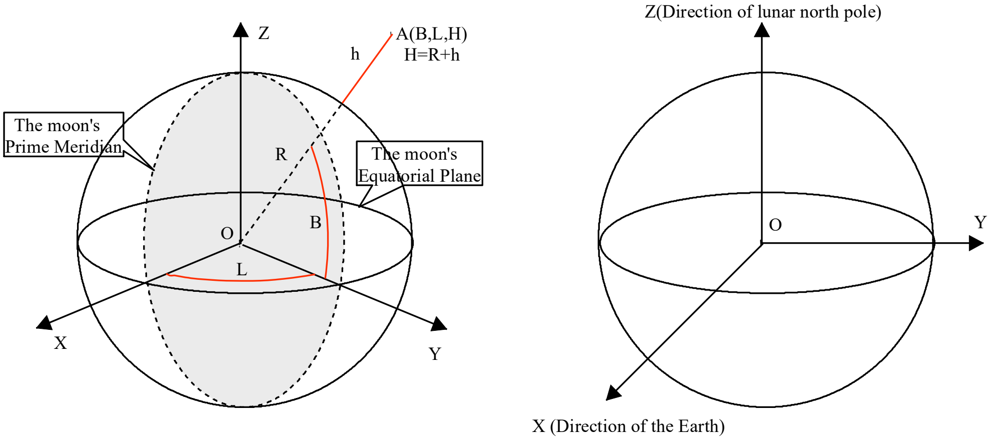

(**a**) (**b**)

Figure 1. Spatial schematic map of lunar geographic coordinate system(**a**) and lunar fixed coordinate system(**b**).

2. The lunar-fixed system;

The lunar-fixed system describes the location of a station on the lunar surface. The lunar-fixed system coordinate system is a right-handed Cartesian system (X, Y, Z; Figure 1(**b**)). The origin is at the lunar centre of mass, the Z-axis is on the line between the North and South Poles, with positive values increasing northward and the X and Y axes are on the plane of the Equator. The X-axis is found by extending from 180 degrees longitude at the Equator (negative) to 0 degrees longitude (prime meridian) at the Equator (positive). The Y-axis is found by extending from 90 degrees west longitude at the Equator (negative) to 90 degrees east longitude at the Equator (positive).

3. Instantaneous coordinate system;

The instantaneous coordinate system is included in the instantaneous projection coordinate system (O-Y′Z′) and three-dimensional instantaneous coordinate system (O-X′Y′Z′; Figure 2). The pointE is the centroid of the earth, the point M is the centroid of the moon, the point D is an arbitrary observation point on the surface of the earth, and the shaded portion is the projection plane at the observation time (Figure2). The origin of the instantaneous coordinate system is O which is the intersection of the observation direction vector DM and the projection surface OY′Z′. The X-axis (OX′) is in the opposite of the observation direction. The Y-axis (OY′) and the Z-axis (OZ′) axes are in the projection plane. The Y-axis is the Normal vector to the plane ODE. The Z-axis could be defined using the right-hand corkscrew rule based on the direction of the X-axis and the Y-axis.

doi:10.20944/preprints202307.1508.v1

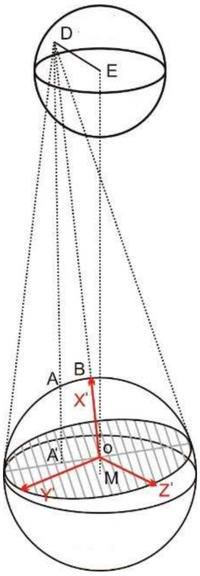

Figure 2. Spatial schematic diagram of the instantaneous coordinate system.

2.2. Methods

In this paper, we focus on observation simulation based on two key information sources: the lunar surface reflectance simulation and a projection transformation from the lunar geographic coordinate system to the instantaneous projection coordinate system that produced fine temporal and high-frequency resolution Lunar reflectance images. The Hapke model is determined for lunar surface reflectance simulation in specific frequency channels and at a specific time. The projection in an instantaneous projection coordinate system can establish a mapped relationship between transformation from the lunar geographic coordinate system and the instantaneous projection coordinate system at the observation time.

2.2.1. Hapke Model

The Hapke bidirectional reflectance model has been widely used for soil modelling. Through this model, the solution of the reflectivity in the direction of the whole moon at the observation time can be realized. I/F, which is also called the radiance factor [22], is the ratio of the radiance observed from a surface to that of a perfectly white Lambertian surface illuminated by the same light, but at normal incidence. I is the radiance data observed from the scene and F is the incident solar irradiance from above the Martian surface. Assuming that the shadow effect is not considered, the equation [19,23] is written as:

$$\frac{I}{F} = LS(i_e,e_e)K\frac{w}{4}\left[p(g)\big(1+B_{S0}B_S(g)\big)+M(i_e,e_e)\right]\left[1+B_{C0}B_C(g)\right] \tag{1}$$

where $LS(i_e,e_e)$ is the Lommel-Seeliger function, i_e and e_e are the effective angle of incidence and emission respectively, K is the porosity factor, w is the single scattering albedo, p(g) is the phase function, B_{S0} is the amplitude of Shadow Hiding Opposition Effect (SHOE), $B_S(g)$ is SHOE function, $M(i_e,e_e)$ is Isotropic Multiple-Scattering Approximation (IMSA) [24,25], B_{C0} is the amplitude of Coherent Backscatter Opposition Effect (CBOE), $B_C(g)$ is Coherent Backscatter Opposition function.

The Lommel-Seeliger function (LS) is given by

$$LS(i_e,e_e) = \frac{\cos(i_e)}{\cos(i_e)+\cos(e_e)} \tag{2}$$

The phase function p(g) is given by

$$p(g) = \frac{1+c}{2}\frac{1-b^2}{(1-2b\cos(g)+b^2)^{3/2}} + \frac{1-c}{2}\frac{1-b^2}{(1+2b\cos(g)+b^2)^{3/2}} \tag{3}$$

where b (0 ≤ b ≤ 1) is the shape-controlling parameter, and c (−1 ≤ c ≤ 1) is the relative strength of backward and forward lobes. The SHOE function $B_S(g)$ is given by

$$B_{S(g)} = 1/[1 + \tan\left(\frac{g}{2}\right)/h_S] \tag{4}$$

where h_S is the angular width parameter of SHOE. The IMSA function $M(i_e, e_e)$ is given by

$$M(i_e, e_e) = H\left(\frac{\cos(i_e)}{K}, w\right) H\left(\frac{\cos(e_e)}{K}, w\right) - 1 \tag{5}$$

where $H(x, w)$ is Ambartsumian-Chandrasekhar H function, which is approximated by

$$H(x, w) \ \simeq \ \{1 - wx[r_0 + \frac{1-2r_0x}{2} \ln\left(\frac{1+x}{x}\right)]\}^{-1} \tag{6}$$

where r_0 is diffusive reflectance, given by

$$r_0 = \frac{1-\sqrt{1-w}}{1+\sqrt{1-w}} \tag{7}$$

The CBOE function $B_C(g)$ is given by

$$B_C(g) = \frac{1+\frac{1-\exp\left[-\tan\left(\frac{g}{2}\right)/h_C\right]}{\tan\left(\frac{g}{2}\right)/h_C}}{2[1+\tan\left(\frac{g}{2}\right)/h_C]^2} \tag{8}$$

where h_C is the angular width of CBOE.

2.2.2. The transformation relationship of the basic coordinate systems

The conversion relationship between the instantaneous projection and lunar geographic coordinate systems was obtained based on using the lunar fixed coordinate system as an auxiliary. The accurate conversion of lunar geographic coordinates to instantaneous projection coordinates was obtained by rotation transformation. This method involves a process of transforming lunar geodetic coordinates to lunar fixed coordinates, lunar fixed coordinates to three-dimensional instantaneous coordinates and, finally, three-dimensional instantaneous coordinates to instantaneous projection coordinates.

1. Transformation of lunar geodetic coordinates to lunar fixed coordinates;

The transformation from the lunar geodetic coordinate system (B, L, H) to the lunar fixed coordinate system (X, Y, Z) to which both can be defined in the lunar ellipsoid is:

$$\begin{cases} X = (R+h)\cdot\cos B\cdot\cos L \\ Y = (R+h)\cdot\cos B\cdot\sin L \\ Z = (R+h)\cdot\sin B \end{cases} \tag{9}$$

where X, Y, Z is the coordinate value corresponding to the lunar point in the lunar fixed system, R is the lunar radius, L, B, h represent the coordinate value of the lunar point in the lunar geographic coordinate system, where L is the longitude and B is the latitude, and h is the elevation.

2. Transformation of lunar fixed coordinates to three-dimensional instantaneous coordinates;

The triaxial vector direction of the instantaneous coordinate system can be expressed in the lunar fixed coordinate system.

The component along the X-axis ($\overrightarrow{MD}$):

$$(X_{X'}, Y_{Y'}, Z_{Z'}) = (X_D, Y_D, Z_D) \tag{10}$$

The component along the Y-axis ($\overrightarrow{OY'}$):

$$\overrightarrow{OY'} = \overrightarrow{MD} \times \overrightarrow{ME}$$

$$(X_{Y'}, Y_{Y'}, Z_{Y'}) = (Y_D Z_E - Z_D Y_E, X_E Z_D - X_D Z_E, X_D Y_E - X_E Y_D) \tag{11}$$

The component along the Z-axis ($\overrightarrow{OZ'}$):

$$\overrightarrow{OZ'} = \overrightarrow{MB} \times \overrightarrow{OY'}$$
$$(X_{Z'}, Y_{Z'}, Z_{Z'}) = (Y_E Z_{Y'} - Z_E Y_{Y'}, X_{Y'} Z_E - X_E Z_{Y'}, X_E Y_{Y'} - X_{Y'} Y_E) \tag{12}$$

The origin of the instantaneous coordinate system in the lunar fixed coordinate system is derived from:

$$\frac{|MO|}{|MH|} = \frac{|MH|}{|MD|}$$
$$|MO| = \frac{|MH| * |MH|}{|MD|} \tag{13}$$

where DH is the tangent line to the moon which passes through the observation station, OH is the radius of the lunar projection circle from the observation station at observation time, and MO is the distance of the Lunar centroid and point M (Figure 3). Point O and B are both on the vector MD, then the point O in the lunar fixed coordinate system is written as:

$$O(O_x, O_y, O_z) = (|MO|, 0, 0) \tag{14}$$

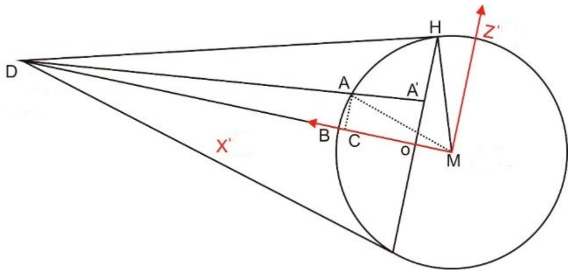

Figure 3. A schematic diagram of the O coordinates for the centre of the projection plane.

The instantaneous coordinate system is defined as taking the site O for origin, (X_{ox}, Y_{ox}, Z_{ox}) for X-axis, (X_{oy}, Y_{oy}, Z_{oy}) for Y-axis, (X_{oz}, Y_{oz}, Z_{oz}) for Z-axis. Here the triaxial unit vector of the lunar fixed coordinate system is written as:

$$X_{ox} = \frac{X_{X'}}{\sqrt{X_{X'}^2 + Y_{X'}^2 + Z_{X'}^2}}, Y_{ox} = \frac{Y_{X'}}{\sqrt{X_{X'}^2 + Y_{X'}^2 + Z_{X'}^2}}, Z_{ox} = \frac{Z_{X'}}{\sqrt{X_{X'}^2 + Y_{X'}^2 + Z_{X'}^2}}$$
$$X_{oy} = \frac{X_{Y'}}{\sqrt{X_{Y'}^2 + Y_{Y'}^2 + Z_{Y'}^2}}, Y_{oy} = \frac{Y_{Y'}}{\sqrt{X_{Y'}^2 + Y_{Y'}^2 + Z_{Y'}^2}}, Z_{oy} = \frac{Z_{Y'}}{\sqrt{X_{Y'}^2 + Y_{Y'}^2 + Z_{Y'}^2}}$$
$$X_{oz} = \frac{X_{z'}}{\sqrt{X_{z'}^2 + Y_{z'}^2 + Z_{z'}^2}}, Y_{oz} = \frac{Y_{z'}}{\sqrt{X_{z'}^2 + Y_{z'}^2 + Z_{z'}^2}}, Z_{oz} = \frac{Z_{z'}}{\sqrt{X_{z'}^2 + Y_{z'}^2 + Z_{z'}^2}} \tag{15}$$

There is simple translation relation between the instantaneous coordinate system and the lunar fixed coordinate system. M was obtained as the rotation matrix in equation (15) from the rotation matrix:

$$M = \begin{bmatrix} X_{ox} & Y_{ox} & Z_{ox} & O_x \\ X_{oy} & Y_{oy} & Z_{oy} & O_y \\ X_{oz} & Y_{oz} & Z_{oz} & O_z \\ 0 & 0 & 0 & 1 \end{bmatrix} \tag{16}$$

According to the definition of the rotation matrix, it can be converted to the lunar fixed coordinate system by rotation transformation in equation (16):

$$(x', y', z', 1) = (x, y, z, 1) \cdot M \tag{17}$$

where (x, y, z) is the target point at the lunar fixed coordinate and (x', y', z') is the target point at the instantaneous coordinate system.

3. Transformation of three-dimensional instantaneous coordinates to instantaneous projection plane coordinates;

The corresponding three-dimensional instantaneous coordinates can be projected to the instantaneous projection coordinates at the observation time by a perspective projection which is a linear projection where there are three-dimensional objects on a projection plane. In the three-dimensional instantaneous coordinate system, the linear equation of each lunar surface site at the observation time was determined to calculate the two-dimensional instantaneous projection coordinate of the target point. The linear equation of the arbitrary sampling point, A, on the lunar surface and the observation point, D, was determined to calculate the intersection coordinates of DA and the projection surface (X=0; Figure 2). The three-dimensional instantaneous coordinate of the intersection point is $(0, Y, Z)$, with an instantaneous projection coordinate of (Y, Z).

3. Results and Discussion

3.1. Observation Environment

The simulated observation site in the study is set in Inner Mongolia, China (115º15΄1.8"east, 42º12΄42.6" north, 1365 m altitude), which is mainly to facilitate the comparative observation requirements later. Different simulation observation points also could be selected according to different observation requirements, and the selection of observation positions here would not affect the accuracy of the research. The coordinates of the observation station in the lunar fixed coordinate system are the basis for the research of the lunar observation geometry. The fundamental ephemerides are the bases for computing the planetary and lunar positions and other related phenomena that are listed in the Astronomical Almanac. The fundamental planetary and lunar ephemerides of the Astronomical Almanac, starting in the year 2003, are DE405/LE405 of Caltech's Jet Propulsion Laboratory (JPL). The coordinates of the observation and the sun are obtained by DE405 during February 2019 (Table 1).

This study used observations from February 10, 2019, and February 19, 2019, as examples. The coordinates of the ground observation are (395850181.233, −40592333.726, 52381084.201) and (357730461.395, −8793065.875, −11557451.723) and the coordinates of the sun are (−68763558072.833, 130348136839.307, −1647761867.411) and (146594202092.887, 21709548884.399, −2268854787.204) (Table 1).

Table 1. Coordinates of observation station and sun in the lunar fixed coordinate system.

Data	**Coordinates of ground observation station**			**Coordinates of the sun**		
	X	**Y**	**Z**	**X**	**Y**	**Z**
2019/2/1	395639321.307	38266042.153	-15849967.443	-99334958891.534	-108485879852.694	-1171442964.620
2019/2/2	399640093.024	30777392.101	-6563094.663	-119974203729.788	-85057374185.770	-1231368074.096
2019/2/3	402685070.881	22136782.712	3300020.343	-135216339462.342	-57802203851.536	-1288816108.819
2019/2/4	404693614.330	12731899.257	13281732.483	-144374909882.550	-27942575832.102	-1344004947.971
2019/2/5	405640480.936	2928981.481	22929598.868	-147036292818.152	3181752374.513	-1397161309.976
2019/2/6	405541552.787	-6930590.156	31810331.329	-143078435155.000	34173595168.771	-1448580728.712
2019/2/7	404440889.456	-16525313.441	39523064.133	-132676493008.997	63641084625.959	-1498682229.099
2019/2/8	402402105.046	-25543546.654	45711628.386	-116295112933.068	90260214900.542	-1548047213.407
2019/2/9	399505457.430	-33672735.027	50075703.091	-94667693940.652	112834367682.262	-1597433863.658
2019/2/10	395850181.233	-40592333.726	52381084.201	-68763558072.833	130348136839.307	-1647761867.411
2019/2/11	391559903.599	-45974249.023	52469735.772	-39744503333.340	142013026479.114	-1700064966.986
2019/2/12	386787918.572	-49493363.868	50270509.901	-8912690818.860	147302963299.864	-1755411786.303
2019/2/13	381719057.508	-50849055.971	45811310.726	22347792041.978	145978021923.941	-1814797129.357
2019/2/14	376566083.558	-49796904.064	39232712.489	52633065902.452	138095292018.467	-1879008847.484

2019/2/15	371560773.505	-46188109.262	30801448.213	80582499483.860	124006394512.285	-1948480187.702
2019/2/16	366942382.327	-40012367.109	20919690.691	104939820676.515	104341757089.059	-2023149071.275
2019/2/17	362947605.099	-31437617.178	10123197.305	124609551347.494	79982360586.191	-2102357053.840
2019/2/18	359804790.386	-20837224.395	-940149.502	138706228121.825	52020241616.223	-2184840665.057
2019/2/19	357730461.395	-8793065.875	-11557451.723	146594202092.887	21709548884.399	-2268854787.204
2019/2/20	356920641.971	3935406.505	-21021437.531	147916241856.587	-9589629379.677	-2352435667.788
2019/2/21	357528505.274	16478337.064	-28710924.878	142609676191.742	-40472151539.559	-2433736968.225
2019/2/22	359627293.264	27949141.862	-34159777.298	130909369199.958	-69550729352.054	-2511328325.223
2019/2/23	363169664.415	37545333.070	-37096038.251	113337395800.903	-95518093425.997	-2584351169.953
2019/2/24	367961943.748	44635701.859	-37445541.630	90679860686.103	-117205674881.443	-2652508169.417
2019/2/25	373667897.489	48819362.226	-35307649.051	63951866322.691	-133636184478.287	-2715928989.419
2019/2/26	379844747.389	49950975.964	-30917152.876	34352166533.880	-144067710609.959	-2774991214.582
2019/2/27	386002345.951	48133405.680	-24604863.636	3209512005.569	-148027322897.020	-2830157031.899
2019/2/28	391670335.457	43683136.367	-16764082.161	-28076922033.176	-145332636386.792	-2881855373.510
2019/3/1	396458241.465	37076022.056	-7825065.961	-58100360361.126	-136100336125.527	-2930415269.263

The equation of the transformation from rectangular coordinates to spherical coordinates is written as:

$$\alpha = \arctan\left(Y/X\right) \ \delta = \arctan\left(\frac{Z}{\sqrt{X^2+Y^2}}\right) \tag{18}$$

where α is the latitude of the subsolar point on the moon, and δ is the longitude of the subsolar point on the moon. Therefore, the spherical coordinates of the subsolar points are (−62.2182, −0.6409) on February 10, 2019, and (8.4281, −0.8776) on February 19, 2019.

3.2. Lunar spectral irradiances simulation

To extract the distribution of instantaneous lunar spectral radiance, the directional reflectance at the observation moment must be obtained first. We would use the MDREMP which gives the directional reflectance of a 30-degree incidence and 0-degree emission angle as the basic data of reflectance simulation in this research. On this basis, we calculated the radiance factor in the standard angle of phase (g) = incidence (i) = 30°, emission (e) = 0° and the radiance factor of each pixel at the observation time by Hapke bidirectional reflectance function using SDRPHO. The standared directional reflectance and the standard radiance factor are shown based on the GCS_MOON_2000 coordinate system in Figure 4 and Figure 5.

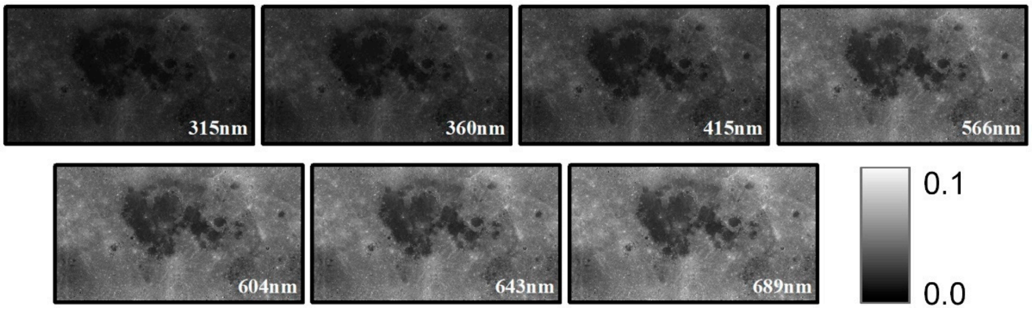

Figure 4. The standard spectral directional reflectance in the angle of phase (g) = incidence (i) = 30°, emission (e) = 0°.

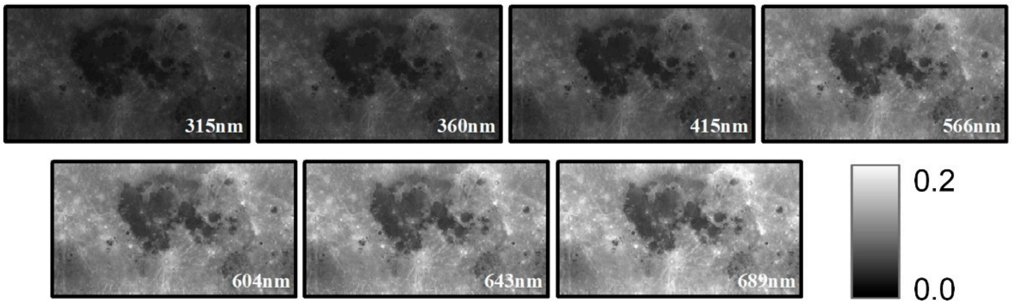

Figure 5. The spectral radiance factor in the angle of phase (g) = incidence (i) = 30°, emission (e) = 0°.

The directional reflectance of each pixel at the observation time is affected by the observation parameters mainly including the incident angle and the emission angle. Since the distance between the earth and the moon is relatively large relative to the radius of the earth, the emission angle is can be approximately 0°, and the function of the incident angle is given by

$$sinh = \ sin\varphi * sin\delta + cos\varphi * cos\delta * cost \tag{19}$$

where δ is the solar declination (equal to the latitude of the subsolar point), φ is the latitude and t is the local time which can be obtained from the subsolar point and the longitude. The distribution of the radiance factor on February 19, 2019, and February 10, 2019, is shown in Figure S1. On February 19, 2019, the subsolar point is close to the prime meridian. Therefore, the lunar phase is close to the full moon and the brightness temperature is high on the near side of the moon. On February 10, 2019, the longitude of the subsolar point is −62.2182 which is also the point of the highest physical temperature.

The lunar spectral reflectance at the observation time is given by

$$Ref_{observation} = \frac{\mathrm{I/F_{observation}}}{\mathrm{I/F_{std}}} * Ref_{std} \tag{20}$$

where $\mathrm{I/F_{std}}$ is the radiance factor in the angle of phase (g) = incidence (i) = 30°, emission (e) = 0°, $\mathrm{I/F_{observation}}$ is the radiance factor of each pixel at the time of observation and $\mathrm{Ref_{std}}$ is the directional reflectivity of 30-degree incident angle and 0-degree emission angle. The solar irradiance at the observation time is written as:

$$I_{observation} = I_{std} * (1AU/d_{Sun-Moon})^2 \tag{21}$$

where $d_{Sun-Moon}$ is the distance between the sun and the moon at the observation time, and I_{std} is the solar irradiance at standardized distances of 1 AU for the Sun and Moon distance. The SOR3SIMD shows that the solar irradiances in 321, 360, 415, 566, 604, 643 and 689nm on February 19, 2019, are 0.6032033, 0.9699519, 1.78526, 1.843822, 1.751854, 1.598708, 1.453432 and the ones on February 10, 2019, are 0.6004955, 0.9693273, 1.785617, 1.843921, 1.752042, 1.598314, 1.453312 in Figure A3. We multiply the solar irradiance by the lunar directional reflectance at the observation time to get the distribution of the lunar surface irradiance at the observation time(Figure 6 and Figure 7).

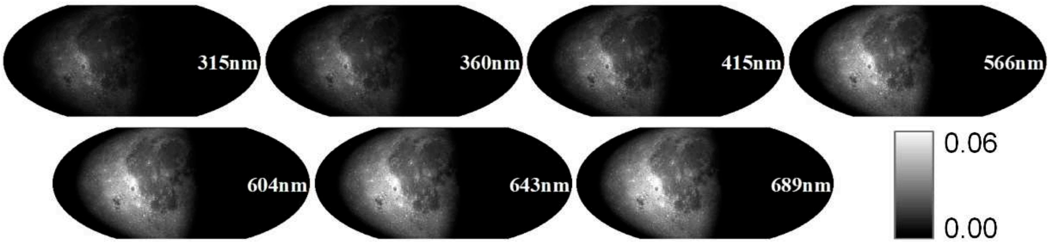

Figure 6. the lunar spetral directional reflectance on February 10, 2019.

doi:10.20944/preprints202307.1508.v1

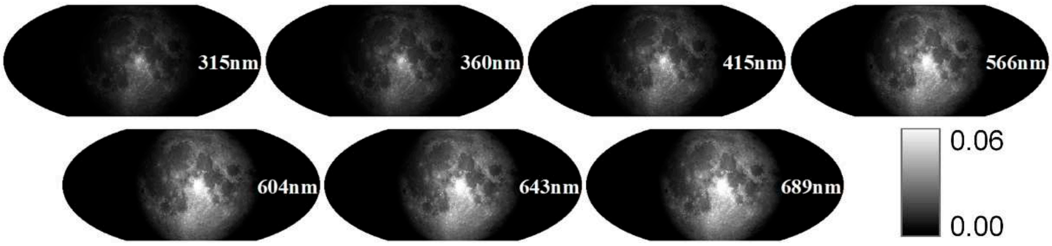

Figure 7. the lunar spetral directional reflectance on February 19, 2019.

3.3. The Earth-based Moon observation geometry

The emission angle of the lunar directional reflectance varies little on each pixel of the moon, for the distance between the earth and the moon is much greater than the radius of the moon. To reduce the computational complexity of the model, the numerical simulation process in this study is approximately vertical observation, that is, the emission angle is 0°. We only need to consider the influence of the observation position and field of view in the simulation. The projection at the observation time in the instantaneous projection coordinate system can be obtained based on transformation from lunar geographic and instantaneous projection coordinate systems on February 10, 2019(Figure 8) and February 19, 2019 (Figure 9). The simulated observation on February 19, 2019, is high at a full moon while most of the Moon's disc is illuminated (Figure 9). While the longitude of the subsolar point is −62.2182 on February 10, 2019, more than half of the moon's disc is unilluminated and the simulated lunar spectral irradiances show low values at the west side of the moon (Figure 8).

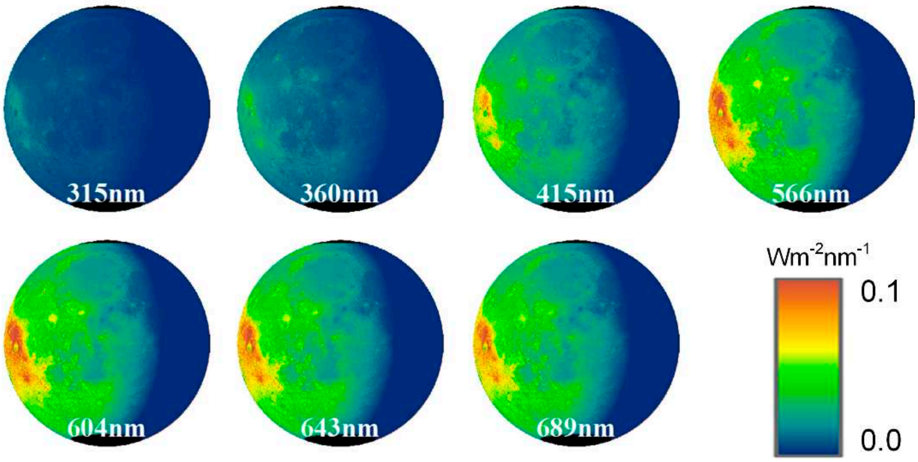

Figure 8. The lunar projection of simulated lunar spectral irradiances on February 10, 2019.

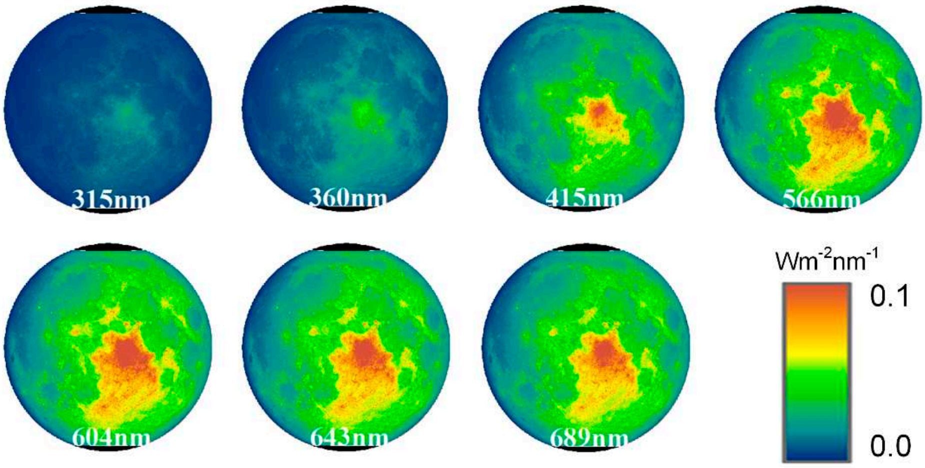

Figure 9. The lunar projection of simulated lunar spectral irradiances on February 19, 2019.

4. Conclusions

In this study, we simulated the distribution of the instantaneous lunar spectral irradiances and established a geometric model for earth-based moon observation. We simulated the lunar observation environment at a specific time point and a specific observation location to obtain the lunar spectral irradiances distribution within the observation field of view. This research can provide technical support for earth-based moon exploration and satellite radiometric calibration. The main conclusions include:

(1) We obtained the lunar bidirectional spectral reflectance at the observation based on the standard reflectance data and reflection factors from product MDRHAP, and product SDRPHO by the Hapke bidirectional reflectance function. And the distribution of the lunar spectral irradiances at the observation time could be achieved based on the lunar bidirectional spectral reflectance and product SOR3SIMD to establish, and finally obtained the product of the lunar albedo at the observation time.

(2) Based on obtaining the distribution of the lunar irradiances at the observation, the conversion relationship between the lunar geographic coordinate system and the lunar fixed coordinate system, the conversion relationship between the lunar fixed coordinate system and the instantaneous coordinate system, and the conversion relationship between the instantaneous coordinate system and the two-dimensional instantaneous projection plane coordinate system was established. Following this, The distribution of the lunar irradiances in the lunar projection plane at the observation time could be obtained quickly, conveniently and accurately. The geometric model for the earth-based moon observation was established in this study.

Author Contributions: YL-Software, Formal analysis, Methodology, Writing - Original Draft, Visualization, Funding acquisition; QR- Conceptualization, Methodology, Visualization, Supervision, Writing - Review & Editing, Funding acquisition; TT, HZ, WL, HG- Data Curation, Formal analysis; JP, ZM - Methodology, Writing - Review & Editing.

Funding: Please add: This study was funded by National Natural Science Foundation of China (Grant No. 41971306), the Foundation of Tianjin Normal University (52XB1502, 043-135202XK1604), National key research and development program of China(2021YFA0715100, 2021YFA0715101).

Institutional Review Board Statement: Not applicable.

Informed Consent Statement: Not applicable.

Data Availability Statement: The data presented in this study are available on request from the corresponding author.

Conflicts of Interest: The authors declare no conflict of interest.

Appendix A

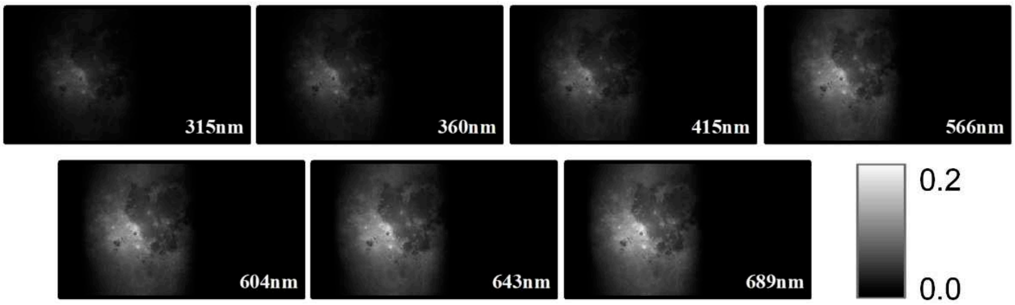

Figure A1. The distribution of the spectral radiance factor on February 10, 2019.

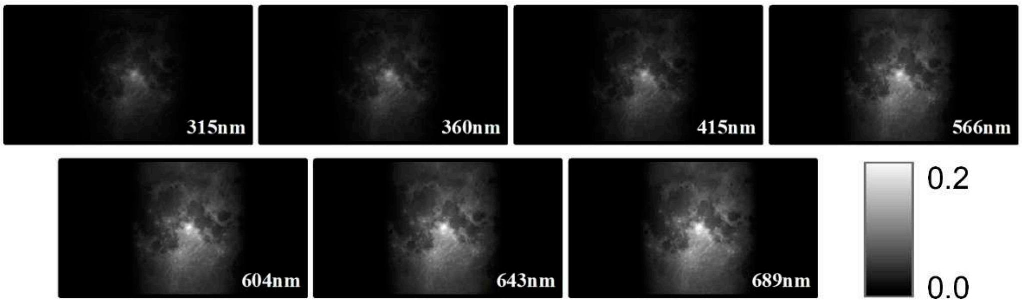

Figure A2. The distribution of the spectral radiance factor on February 19, 2019.

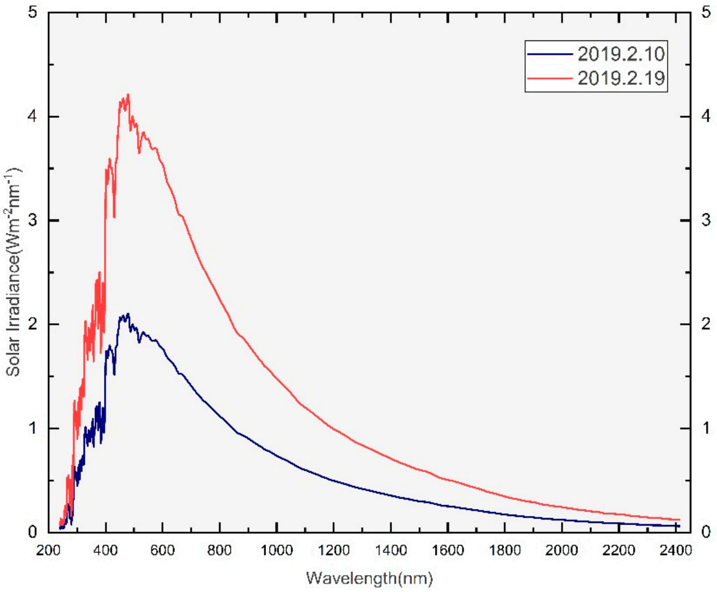

Figure A3. SOR3SIMD SORCE Spectral Irradiance at the observation time.

References

1. Green P D and Lobb D. 2015. The traceable radiometry underpinning terrestrial and helio studies (truths) mission//Proceedings of SPIE 9639, Sensors, Systems, and Next-Generation Satellites XIX. Toulouse: SPIE: 96391C [DOI: 10.1117/12.2192593]
2. Leckey J. 2015. Climate absolute radiance and refractivity observatory (CLARREO). International Archives of the Photogrammetry, Remote Sensing and Spatial Information Sciences, XL-7/W3: 213–217 [DOI: 10.5194/isprsarchives-XL-7-W3-213-2015]
3. Kieffer H H and Wildey R L. **1985.** Absolute calibration of landsat instruments using the moon. *Photogrammetric Engineering and Remote Sensing*, *51(9)*: 1391–1393
4. Kieffer H H. **1997**. Photometric stability of the lunar surface. *Icarus*, *130(2)*: 323–327 [DOI: 10.1006/icar.1997.5822]
5. Kouyama T, Yokota Y, Ishihara Y, et al. Development of an application scheme for the SELENE SP lunar reflectance model for radiometric calibration of hyperspectral and multispectral sensors[J]. *Planetary and Space Science*, **2016**,*124*:76～83.
6. Kieffer H H, Wildey R L. Establishing the Moon as a Spectral Radiance Standard[J]. *Journal of Atmospheric and Oceanic Technology*,**1996**,*13(2)*:360～375.
7. Kieffer H H, Stone T C. The spectral irradiance of the moon[J]. *Astronomical Journal*, **2005**,*129(6)*:2887.
8. Stone T C. Radiometric calibration stability and inter-calibration of solar-band instruments in orbit using the moon[J]. *Proceedings of SPIE -The International Society for Optical Engineering*, **2008**, *7081*:70810X～70810X-9.
9. Zhang L, Zhang P, Hu X, et al. A novel hyperspectral lunar irradiance model based on ROLO and mean equigonal albedo[J]. *Optik - International Journal for Light and Electron Optics*, **2017**, *142(2017)*:657～664
10. Sun J Q, Xiong X, Barnes W L, et al. MODIS Reflective Solar Bands On-Orbit Lunar Calibration[J]. *IEEE Transactions on Geoscience & Remote Sensing*, **2007**, *45(7)*:2383～2393.
11. Kieffer H H, Jarecke P J, Pearlman J. Initial lunar calibration observations by the EO-1 Hyperion imaging spectrometer[J]. *Proceedings of SPIE - The International Society for Optical Engineering*, **2002**, *4480*:43～253.

12. tone T C, Kieffer H H, Grant I F. Potential for calibration of geostationary meteorological satellite imagers using the Moon[J]. *Proc. Of SPIE - The International Society for Optical Engineering*, **2005**, *5882*:58820P-1～58820P-9.
13. Barnes R A, Eplee R E, Patt F S Jr, et al. Changes in the radiometric sensitivity of SeaWiFS determined from lunar and solar-based measurements[J]. *Applied Optics*, **1999**, *38(21)*:4649-64.
14. Barnes W, Xiong M X, Eplee M R, et al. Use of the Moon for Calibration and Characterization of MODIS, SeaWiFS, and VIRS[J]. *Neuropharmacology*, **2006**, *30(12A)*:1269～74.
15. Xiong X, Butler J, Chiang K, et al. Assessment of S-NPP VIIRS On-Orbit Radiometric Calibration and Performance[J]. *Remote Sensing*, **2016**, 8(2).
16. Kouyama T, Kato S, Miyashita N. One-year lunar calibration result of Hodoyoshi-1, Moon as an ideal target for small satellite radiometric calibration[C]. 32nd Annual AIAA/USU Conference on Small Satellites, 2018.
17. Wu Ronghua, Zhang Peng, Yang Zhongdong, et al. Monitor the radiance calibration of the remotesensing instrument by using the reflected lunar irradiance[J]. *Journal of Remote Sensing*, **2016**, *20(2)*: 278～289.
18. Robinson M S, Brylow S M, Tschimmel M, et al. Lunar reconnaissance orbiter camera (LROC) instrument overview[J]. *Space science reviews*, **2010**, *150(1)*: 81-124.
19. Sato, H., Robinson, M.S., Hapke, B., Denevi, B.W., Boyd, A.K. (**2014**) Resolved Hapke parameter maps of the Moon. *Journal of Geophysical Research Planets*, *119*, 1775–1805. doi:10.1002/2013JE004580.
20. Boyd A K, Robinson M S, Sato H. Lunar Reconnaissance Orbiter wide angle camera photometry: An empirical solution[C]//*Lunar and planetary science conference*. **2012** *(1659)*: 2795.
21. Cahalan R F, Ajiquichí P, Yatáz G. Solar Temperature Variations Computed from SORCE SIM Irradiances Observed During 2003–2020[J]. *Solar Physics*, **2022**, *297(1)*: 1-37.
22. Hapke, B. 1993, *Theory of Reflectance and Emittance Spectroscopy* (New York: Cambridge Univ. Press), 262
23. Hapke, B. (2012), *Theory of Reflectance and Emittance Spectroscopy*, Cambridge Univ. Press, New York.
24. Hapke, B. (1981), *Bidirectional reflectance spectroscopy*: 1. Theory, J. Geophys. Res., 86(B4), 3039–3054, doi:10.1029/JB086iB04p03039.
25. Hapke, B. (**1999**), Scattering and diffraction of light by particles in planetary regoliths, *J. Quant. Spectrosc. Radiat. Transfer*, *61(5)*, 565–581.